

First characterization of silicon crystalline fibers produced with the μ -pulling technique for future gravitational wave detectors

M. Alshourbagy

Istituto Nazionale di Fisica, Sezione di Pisa, Pisa, Italy, and Dipartimento di Fisica, Universita di Pisa, Pisa, Italy

P. Amico and L. Bosi

Istituto Nazionale di Fisica Nucleare, Sezione di Perugia, I-06100 Perugia, Italy, and Dipartimento di Fisica, Universita di Perugia, I-06100 Perugia, Italy

G. Cagnoli

Institute for Gravitational Research, Department of Physics and Astronomy, University of Glasgow, Glasgow, United Kingdom, Dipartimento di Astronomia e Scienza dello Spazio, Universita di Firenze, 50125 Firenze, Italy, and Istituto Nazionale di Fisica Nucleare, Sezione di Firenze, Firenze, Italy

E. Campagna

Istituto Nazionale di Fisica Nucleare, Sezione di Firenze, Firenze, Italy, and Istituto di Fisica, Universita di Urbino, Urbino, Italy

F. Cottone

Istituto Nazionale di Fisica Nucleare, Sezione di Perugia, I-06100 Perugia, Italy, and Dipartimento di Fisica, Universita di Perugia, I-06100 Perugia, Italy

A. Dari

Istituto Nazionale di Fisica Nucleare, Sezione di Perugia, I-06100 Perugia, Italy, and Dipartimento di Fisica, Universita di Camerino, Camerino, Italy

L. Gammaitoni

Istituto Nazionale di Fisica Nucleare, Sezione di Perugia, I-06100 Perugia, Italy, and Dipartimento di Fisica, Universita di Perugia, I-06100 Perugia, Italy

M. Lorenzini

Istituto Nazionale di Fisica Nucleare, Sezione di Firenze, Firenze, Italy, and Dipartimento di Astronomia e Scienza dello Spazio, Universita di Firenze, 50125 Firenze, Italy

G. Losurdo

Istituto Nazionale di Fisica Nucleare, Sezione di Firenze, Firenze, Italy

F. Marchesoni

Istituto Nazionale di Fisica Nucleare, Sezione di Perugia, I-06100 Perugia, Italy, and Dipartimento di Fisica, Universita di Camerino, Camerino, Italy

F. Martelli and F. Piergiovanni

Istituto Nazionale di Fisica Nucleare, Sezione di Firenze, Firenze, Italy, and Istituto di Fisica, Universita di Urbino, Urbino, Italy

M. Punturo

Istituto Nazionale di Fisica Nucleare, Sezione di Perugia, I-06100 Perugia, Italy

A. Toncelli and M. Tonelli

Istituto Nazionale di Fisica, Sezione di Pisa, Pisa, Italy, and Dipartimento di Fisica, Universita di Pisa, Pisa, Italy

F. Travasso

Istituto Nazionale di Fisica Nucleare, Sezione di Perugia, I-06100 Perugia, Italy, and Dipartimento di Fisica, Universita di Perugia, I-06100 Perugia, Italy

F. Vetrano

Istituto Nazionale di Fisica Nucleare, Sezione di Firenze, Firenze, Italy, and Istituto di Fisica, Universita di Urbino, Urbino, Italy

H. Vocca

Istituto Nazionale di Fisica Nucleare, Sezione di Perugia, I-06100 Perugia, Italy, and Dipartimento di Fisica, Universita di Perugia, I-06100 Perugia, Italy

(Received 9 December 2005; accepted 5 March 2006; published online 19 April 2006)

The design of the gravitational wave interferometric detectors of third generation is under way. An overall improvement of the detector performance can be obtained by reducing a few noise sources, such as seismic noise, shot noise, and most importantly thermal noise. We report here on the design

and fabrication of low thermal-noise suspensions made of a new material presently under investigation. An *ad hoc* technique to produce crystalline silicon fibers has been developed; the first measurements of the fiber mechanical and thermal properties at room temperature have been performed and interpreted. Preliminary measurements of the mechanical losses at low temperature are also discussed. © 2006 American Institute of Physics. [DOI: 10.1063/1.2194486]

I. INTRODUCTION

In the design of advanced gravitational wave (GW) interferometric detectors, thermal noise represents the most serious sensitivity limitation in the frequency range from a few hertz to a few kilohertz. In particular, thermal noise in the suspensions dominates the sensitivity curve up to 100 Hz, while the thermal noise in the test masses is expected to become the main noise source at larger frequencies, i.e., up to 1 or 2 kHz. Structural and thermal relaxation processes are intimately related to volume and temperature fluctuations, which in turn cause random variations of the position and shape of the various mechanical parts of the interferometer. At constant temperature and in a frequency range far from the mechanical resonances, an appreciable reduction of the power spectral density due to thermal noise can be achieved suppressing the mechanical losses.

The suspension system of the main optics in the current GW interferometric detectors is based on a single or double metal wire loop.¹⁻⁵ Only the GEO600 detector uses a different suspension system,⁶ based on a monolithic fused silica design. Fused silica is a good material for low thermal noise suspensions because of its low intrinsic loss angle (ϕ_w) and its low thermoelastic effect.⁷⁻¹²

Crystalline materials have structural losses as low as, or even lower than silica but, due to their relatively large thermal expansion, the thermoelastic loss dominates by far over the sensitive frequency range. For this reason crystalline materials have never been considered suitable for the construction of low thermal-noise suspensions at room temperature.

The thermoelastic loss angle ϕ_{th} of a homogeneous fiber is given by

$$\phi_{th}(f) = \Delta \frac{f\tau_h}{1 + (f\tau_h)^2}, \quad (1)$$

where $\Delta/2$ is the amplitude of the thermoelastic peak. The thermoelastic peak strength Δ is related to the temperature T and to the thermoelastic coefficients of the material, namely, the Young's modulus E , its specific heat per unit volume $c_v(T)$ and, most importantly, its thermal linear expansion coefficient α , through the following expression:^{9,13}

$$\Delta = \frac{E\alpha^2 T}{c_v}. \quad (2)$$

We remind that $c_v(T) = C_V(T)\rho(T)$ ($J\ m^{-3}\ K^{-1}$), where C_V and ρ are, respectively, the specific heat at constant volume and the density of the material. When the material is subjected to a large static stress as in the suspension fibers, the coefficient α must be modified to account for the temperature dependence of Young's modulus.¹⁴ The frequency of the thermoelastic peak is given by $f = 1/\tau_h$, where τ_h is the heat propagation characteristic time, related to the geometry of

the fiber and to the material properties through the thermal conductivity κ . For a cylindrical fiber,

$$\tau_h = \frac{c_v d_w^2}{2.16\kappa}, \quad (3)$$

with d_w denoting the fiber diameter. It has already been pointed out^{15,16} that crystalline silicon is a very promising material for cryogenic interferometric detectors due to the observation that its thermal expansion vanishes in two temperature neighborhoods at around 18 and 123 K.

From Eq. (1) it is also apparent that the fiber loss angle depends on both the frequency $1/\tau_h$ and the strength Δ of the thermoelastic peak. Moreover, in previous work we have reported on the very high thermal conductivity of crystalline silicon at low as well as at room temperature.^{17,18} We have pointed out that silicon can thus be used as a suspension material for room temperature and cryogenic interferometers, alike; indeed, the thermoelastic peak of the suspension fibers in planned GW detectors is expected to occur at very high frequency. The silicon properties are reviewed in Sec. II and a quantitative analysis of the thermoelastic losses in silicon fibers is presented in Sec. III.

A facility for the fiber production has been assembled about two years ago in the Pisa laboratory with the twofold purpose of testing the μ -pulling technique for growing suspension fibers and providing samples for the current research on new suspension materials. The idea is to produce silicon fibers with variable doping and chemical composition, otherwise not available through commercial suppliers. Details of our facility and of the growing method are sketched in Sec. IV.

The thermomechanical and crystallographic characterizations of the first silicon fibers produced by the μ -pulling technique are reported and analyzed in Secs. V (room temperature) and VI (low temperature).

II. SILICON PROPERTIES

Silicon thermal and mechanical properties are extremely favorable to reduce thermal noise in the optics suspensions of a GW interferometric detector. In the frequency range comprised between the pendulum resonance and the first violin mode of the suspension fibers, the power spectral density of the thermal noise displacement of a suspended mirror $|X_p(\omega)|^2$ is well approximated by the following expression:

$$|X_p(\omega)|^2 \simeq \frac{4k_B T}{\omega^5} g \frac{1}{L_f^2} \sqrt{\frac{Eg}{4\pi nm}} \left(\frac{\phi(\omega)}{C_s T_B} \right), \quad (4)$$

where L_f is the suspension fiber length, E is Young's modulus of the fiber material, n is the number of suspension fibers for each mirror of mass m , and C_s is the percentage of tensile

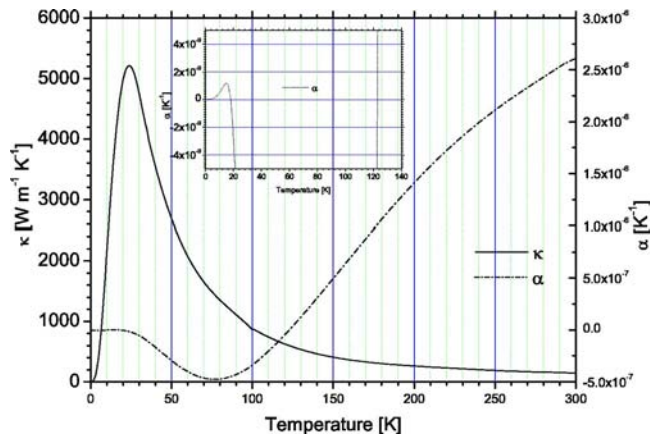


FIG. 1. Thermal conductivity (continuous line) and linear thermal expansion coefficient (dash-dotted line) of silicon Refs. 30 and 31 the two temperatures (about 18 and 123 K) where the thermal expansion coefficient vanishes, as well as the peak of the thermal conductivity at low temperature, are apparent in the plot in the small box.

breaking stress T_B at which the fiber is loaded. The loss angle $\phi(\omega)$ represents the sum of all the dissipative processes that occur in the material (structural and thermoelastic losses) plus an effective loss angle for the losses associated with the connecting elements such as clamps, break-off points, or chemical bonded pieces. Silicon is expected to have large bulk tensile strength (about 7 GPa, dominated by surface effects that can decrease that value down to about 200 MPa Ref. 19) and comfortably low intrinsic loss angle [$\phi_i(300 \text{ K}) \approx 2.8 \times 10^{-8}$, $\phi_i(77 \text{ K}) \approx 5 \times 10^{-9}$, and $\phi_i(4.2 \text{ K}) \approx 6 \times 10^{-10}$].^{20–22} The behavior of the linear thermal expansion coefficient α and of the thermal conductivity κ is peculiar, as displayed in Fig. 1. All the thermomechanical properties of silicon reported in this section (Figs. 1 and 2) are taken from Ref. 23. The thermal expansion coefficient decreases with the temperature until it vanishes at about 123 K, is negative in the temperature interval of (18–123) K, and almost zero at lower temperatures. This means that the thermoelastic dissipation decreases sharply with the temperature and becomes negligible with respect to the structural losses in the range of 120–130 K and below 20 K, as reported in Fig. 3.

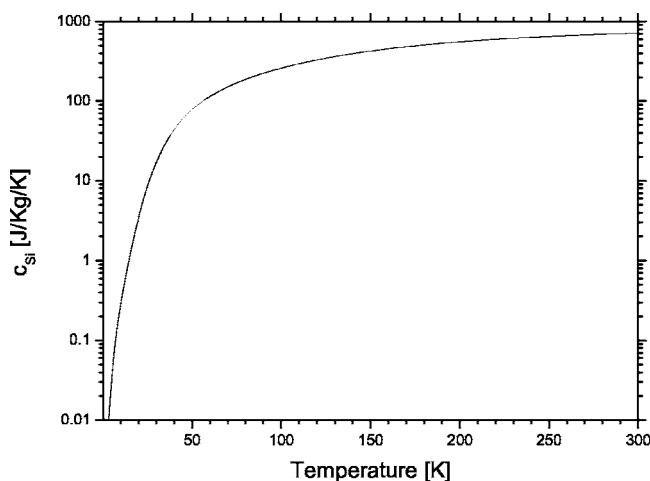


FIG. 2. Specific heat ($\text{J K}^{-1} \text{K}^{-1}$) of silicon (Refs. 23 and 27).

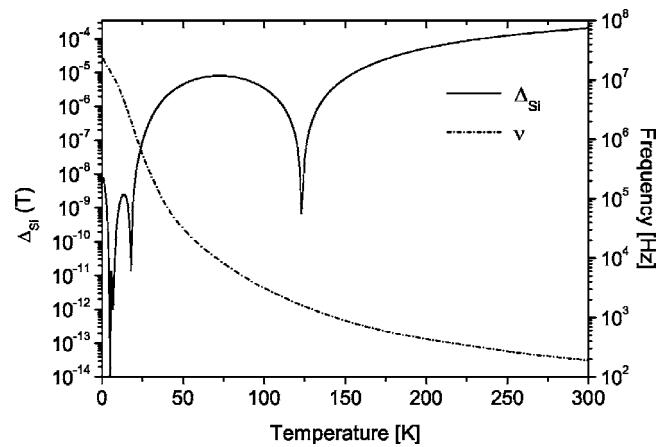


FIG. 3. Amplitude of the linear thermoelastic loss angle in a silicon fiber, computed using Eq. (2) and Ref. 23. Ideally, at the two temperatures where the thermal expansion coefficient vanishes Δ_{Si} is null. The expected temperature dependence of the thermoelastic peak frequency $1/\tau_h$ in a $560 \mu\text{m}$ diam. silicon fiber is also shown. The frequency increase at low temperature should contribute to reduce the thermoelastic dissipation in the suspension.

The thermal conductivity κ of silicon increases at low temperature pushing the thermoelastic peak toward higher frequencies, as shown in Fig. 3 for a silicon fiber of $560 \mu\text{m}$ in diameter. After reaching a maximum, the thermal conductivity drops as the phonon mean free path grows larger than the typical cross section of the sample; see Fig. 1. Note that the thermal conductivity varies greatly with the doping of the material and with the concentration of the lattice defects, so that the curve of Fig. 1 is ought to be taken as a qualitative representation of $\kappa(T)$.

III. THERMOELASTIC LOSS ESTIMATION IN SUSPENSION FIBERS

In this section we compare the thermoelastic losses of different materials. Almost all the present GW interferometric detectors use steel wires to suspend the main optics. This choice provides a convenient solution to keep in position (safely and easily) very expensive optics. In Virgo the wire steel (C85) (Ref. 10) and the suspension design⁴ have been selected to optimize the thermal-noise control. The intrinsic loss angle of C85 steel has been measured to be about 2×10^{-4} , at the best, while many crystalline materials [such as sapphire or yttrium aluminum garnet (YAG)] have intrinsic loss angles well below that value. However, these materials have not been considered for low thermal-noise suspensions because of their large thermal expansion coefficient, which enhances their thermoelastic dissipation. The thermoelastic losses of different materials is compared in Fig. 4. For instance, the advantage in using sapphire fibers is clearly nullified by the dominant thermoelastic loss angle at low frequency. On the contrary, fused silica has an intrinsic loss angle below 10^{-7} – 10^{-8} (depending on the type of fused silica) and, more notably, its thermoelastic dissipation is suppressed by a small thermal expansion coefficient. Finally, Fig. 4 suggests that another material could be selected to realize low thermal-noise suspensions, namely, crystalline silicon. In fact, silicon does have a large thermoelastic peak, but for very high frequencies. This is due to the high thermal

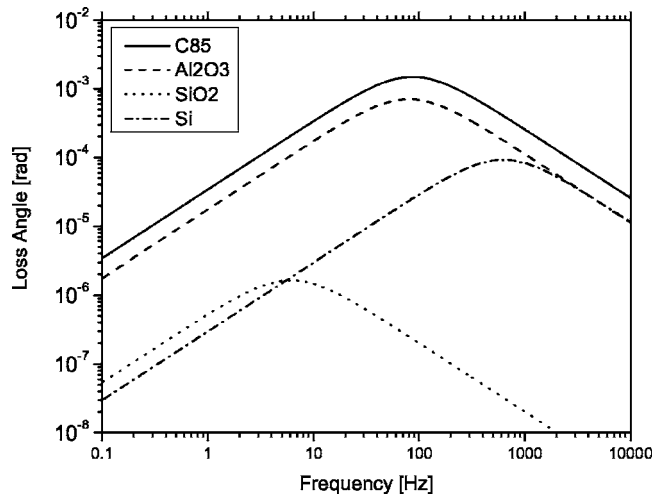


FIG. 4. Expected thermoelastic peaks at room temperature ($T=300$ K) in fibers ($560\ \mu\text{m}$ in diameter) made of C85 steel (solid curve), Ref. 10 sapphire (dashed curve) Ref. 23, fused silica (dotted curve) Refs. 10 and 23, and Silicon (dash-dotted curve) Ref. 23.

conductivity of silicon. As a result, at low frequency, where the thermal noise in the suspensions dominates the noise budget of GW detectors, the thermoelastic dissipation in silicon fibers could be even lower than in fused silica fibers. This effect, together with its low intrinsic loss angle,²⁰ singles out silicon as one of the most promising materials for low thermal-noise suspensions in GW detectors.

IV. PRODUCTION OF SILICON FIBERS

In Sec. I we discussed the reasons for assembling a dedicated facility for the production of suspension fibers. Concerning the fiber geometry there are three aspects to take into account: strength, thermal conduction, and resonance frequencies. The main optics in present and future GW interferometric detectors are massive mirrors (more than 20 kg in Virgo). Safety and reliability are important issues for the suspension fibers. Considering a working load of 200 MPa, each of the four fibers sustaining the mirror should have a diameter of $560\ \mu\text{m}$. For a fiber length of 40 cm the vertical bouncing frequency is about 22 Hz (neglecting any coupling with the rest of the suspension) and the frequency of the corresponding first violin mode is 17 times larger. Without affecting the safety of the suspension system, the vertical bouncing frequency can be reduced by inserting suitable flexural elements also made of silicon.

In a future interferometric detector of gravitational waves the light power circulating in the optical cavities will be so large that about 1 W will be deposited in the suspended optics; it should be noted that the described suspension geometry is not able to extract the deposited energy without causing a too large temperature difference between the optics and the suspension. In fact, the thermal resistance of four such fibers is about 650 K/W assuming a thermal conductivity of $630\ \text{W}/(\text{m K})$, that is approximately the conductivity value expected around 120 K (Fig. 1). This means that a (unrealistic) temperature difference $\Delta T=650$ K between the two ends of the suspension fibers is needed to extract 1 W of

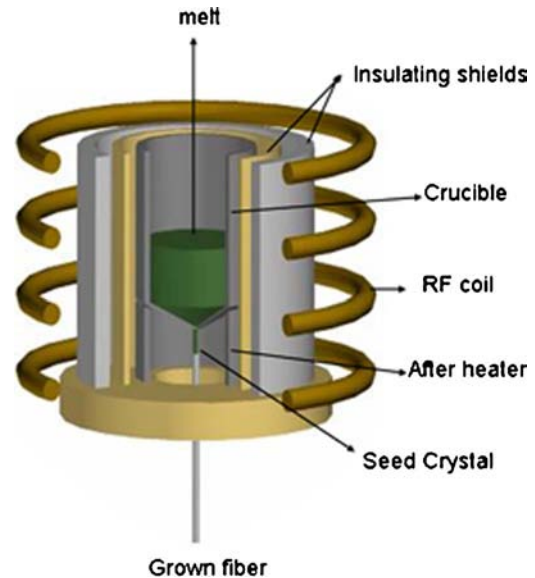


FIG. 5. Schematic diagram for the μ -PD growth apparatus (hot zone part).

light power deposited in the mirror. A further investigation on the design of the suspension elements is necessary.

Silicon fibers similar to those described above have been grown in the Pisa laboratory. There a crystal growth furnace, that uses the so-called micropulling down technique (μ -PD), was set up. Basically the μ -PD method involves downward pulling of a crystal fiber through a micronozzle placed at the bottom of the crucible as shown in Fig. 5. The method allows to grow crystals in shape of fibers, rods or ribbons with diameters in the range of $0.15\text{--}5\ \text{mm}$ at widely variable pulling rates.²⁴ The melt is placed in crucibles made of materials stable at temperatures as high as the melting point of the target crystalline material. The crucibles are heated using a radio-frequency (rf) generator. At the first stage a seed fiber crystal produced from previous experiments or cut from a bulk crystal of the corresponding material is inserted into the crucible orifice. The seed is then pulled downward using an accurate pulling mechanism. Normally the surface forces do not allow the melt to separate from the fiber material. Therefore the melt passes through the nozzle at the bottom of the crucible and the new fiber is grown. Application of an after heater allows adjustment of the appropriate temperature gradients under the crucible and therefore regulation of the position of the solid-liquid interface in the vicinity of the crucible tip. The shape and location of the growth interface is one of the most important parameters determining the quality and uniformity of the resulting crystal. Therefore special attention is normally paid to monitor and detect the spatial distribution of the temperature gradient in the vicinity of the phase boundary. A charge-coupled device (CCD) camera and monitor are considered to be very good tools to view the solid-liquid interface and the meniscus region. The furnace can be evacuated and inert atmosphere can be inserted. The furnace has been tested with several materials and about 20 silicon fibers have already been grown.

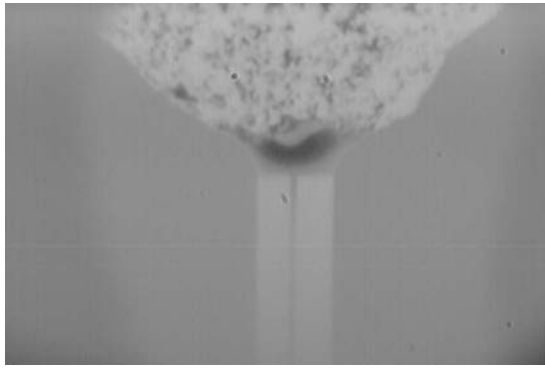


FIG. 6. Image of a fiber during the growth process.

A. Growth process

The starting material was a 5-N (99.999%) purity Si in small pieces of few millimeters. These pieces were inserted in a vitreous carbon crucible. This crucible of about 27 mm in height and 18 mm in diameter was placed on an after heater of the same material and everything was held by a zirconate pedestal in a vertical alumina ceramic tube and was heated using a rf generator. Cylindrical heat shields made of alumina or zirconate ceramics were placed around the crucible as shown in Fig. 5.

The crucible temperature was controlled by the power of the rf coil which has dimensions of about 80 mm length and 70 mm diameter with eight windings, and the furnace maximum operating temperature is around 2100 °C. To avoid the oxidation of the crucible the crystal was grown in Ar gas of 99.999% purity. Visual observation of the meniscus region, solid-liquid interface and the crystal growing was made by a CCD camera and a monitor.

B. Seeding and growth procedure

Several Si single crystals with different lengths and diameters were grown. As a first step, a $\langle 100 \rangle$ oriented thin cut from Si disk was used as a seed. The crystals were grown at various pulling rate from 0.3 to 2 mm/min and were 0.4–3 mm in diameter and 40–310 mm in length. The growth of long crystal fibers is affected by vibrations which become especially intense at longer lengths. It was found that the amplitude of the fiber oscillations also depends on the fiber diameter.²⁵ Disconnection of the fiber growing from the molten zone was never observed, but the growth process was not perfectly stable and some abrupt changes in diameter and/or temperature happened probably due to instabilities of

the rf generator and to reaction between silicon and the crucible that also prevented a good contact between the seed and the melt. Anyway for most of their length the fibers show good quality. Figure 6 shows a moment during the growth of the fiber.

Some typical Si crystal fibers grown with different diameters and lengths are shown in Fig. 7. The crystal orientation of the fibers was determined using the Laue x-ray diffraction method. From this measurement it is possible to say that all the good quality parts of the fibers inspected showed single crystalline character, but it was found that the orientation changes along the fiber length in every point where the diameter is not stable. As a result the fibers are not single crystal along all their length, but they are composed of several single-crystal parts. Optical absorption measurements at wavelengths longer than 1.2 μm did not show the presence of any contaminants within the sensitivity of the apparatus (absorbance of 1%).

V. MEASUREMENTS OF THERMOMECHANICAL PARAMETERS OF FIBERS AT ROOM TEMPERATURE

A. Profile measurement and modeling of the fibers

The shape of the Si fibers produced up to now is not perfectly cylindrical: The diameter varies along the fiber axis resulting in the presence of larger and narrower regions; the transverse section is irregular too. Since it is necessary to model the fiber in order to compare the experimental results with theoretical predictions of thermoelastic losses, a careful measurement of the profiles along the fiber's axis for different angular orientations is needed.

To perform this measurement the shadow of the fiber is projected by a laser beam on a photodiode masked by a narrow rectangular window and placed close to the fiber to minimize diffraction effects. The laser light, modulated at 1360 Hz to get rid of the environmental noise, is also sampled by a beam splitter and focalized on a second photodiode to get a reference signal. The fiber can be moved across the laser beam and rotated around its axis.

The system is always calibrated before acquiring a profile by measuring in the same way a set of cylindrical wires whose diameters are known with an error of $\pm 5 \mu\text{m}$. This error dominates the global error on the fiber profile measurement. A further check of the procedure, measuring a reference fiber segment in a digital picture taken at the microscope, showed a good agreement with the result obtained

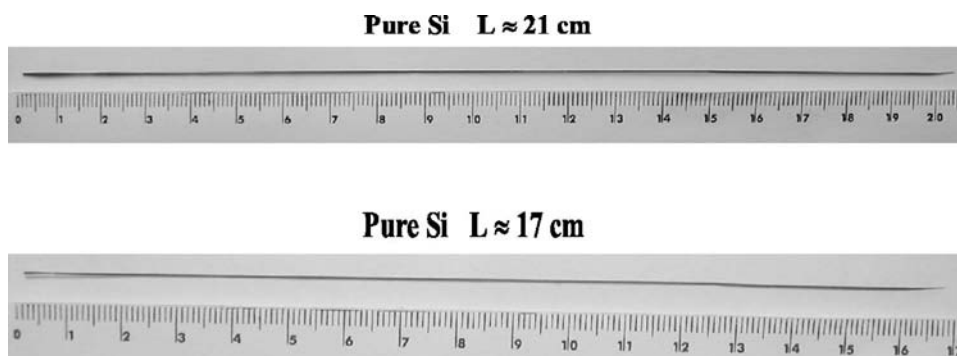


FIG. 7. Grown Si single-crystal fibers ≈ 0.4 mm in diameter and 17 and 21 cm long.

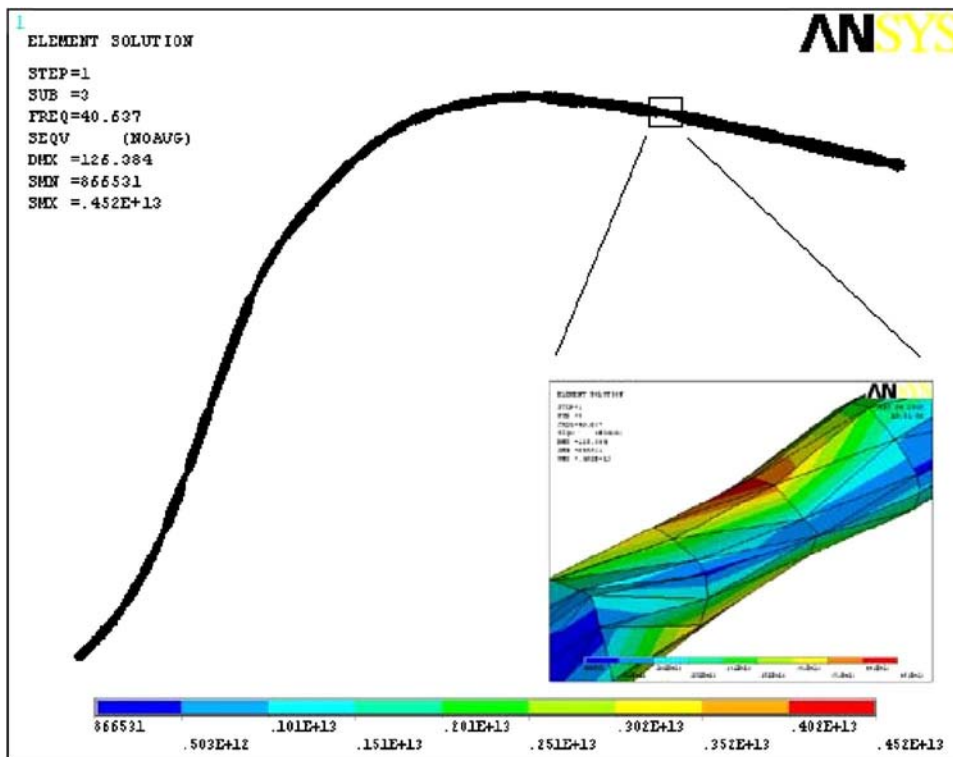


FIG. 8. The simulated second mode of a 308 mm long fiber. In the expanded segment the stress distribution is also visible.

with the laser beam; from this a 3.5% error on the diameters is deduced. The full set of 30°-spaced profiles was measured with a resolution of 0.5 mm along the fiber axis.

These data are used to create a three-dimensional (3D) finite element model (using the ANSYS© software) to simulate the fiber behavior. Firstly the 0.5 mm spaced fiber sections are defined using the 12 measured keypoints; then the various sections are connected by means of a tetrahedral volume mesh. A modal analysis is performed to extract the resonance frequencies of the first 40 modes and their shapes. The clamp is also taken into account by constraining all the degrees of freedom of the fiber at one end. Figure 8 shows the simulation of the second mode of a 308 mm long fiber and the stress distribution in a narrower region.

B. Room temperature measurement of the thermoelastic peak

In order to measure the loss angle at room temperature, the fiber is clamped at one end between two aluminum blocks, fixed to a massive solid structure to keep the recoil losses at a negligible level. The whole structure stays in a vacuum chamber at a residual pressure of 10^{-5} – 10^{-6} mbar. The damping due to residual gas molecules in the vacuum chamber is estimated to be of the order of 10^{-8} .²⁶ Because of the dielectric properties of silicon, it is possible to induce the oscillations of the fiber using a comb capacitor exciter driven by an high voltage oscillating signal. The comb configuration provides a large electric field gradient. The position of the fiber is measured using two side-by-side photodiodes forming a shadow sensor.²⁸

With the above described model of the fiber the resonance frequencies are easily located. Each vibration mode is then excited using a sinusoidal wave at the resonance frequency. The preamplified shadow-sensor signal is sent to a

lock-in amplifier in order to filter the noise and to lower the signal frequency, then it is acquired on a PC. When the exciting signal is removed and the capacitor grounded, it is possible to observe the ring down of the oscillation.

The Hilbert transform of this signal is then used to fit the value of the time constant τ , related to the loss angle by

$$\phi = \frac{1}{\pi f \tau}. \quad (5)$$

For each resonance mode the ϕ evaluation is repeated several times: From the observed dispersion of the measured values an error on ϕ ranging from 1% to 5%, where the contribution coming from the fit is only at the level of 1%, is estimated. The measured values of the loss angle for a 308 mm long fiber are shown in Fig. 9(a). As it will be explained later, from the analysis of these data, the values of Young's modulus E , of the thermal expansion coefficient α and of the thermal conductivity κ , can be evaluated. Using the measured value of E the dispersion relation allows to define an "effective" diameter for each resonance mode. Assuming a cylindrical-shaped fiber with this diameter it is possible to predict a value of the loss angle for each resonance frequency. These predictions, with the error coming mainly from the uncertainty in the diameter measurement, are also shown on Fig. 9. It is quite evident the presence of an excess loss. This excess can be due to contaminants present on the fiber surface: After the production of the fiber, the external surface is, in fact, subject to oxidation; furthermore it is also possible the deposition of some impurities on it during the growing process. To verify this hypothesis a chemical etching process was performed on the fiber, removing the first Si layers. The part of the fiber inside the clamp was not etched: In this way the narrowing of the fiber just outside the clamp can help in further reducing the clamp losses. To obtain an

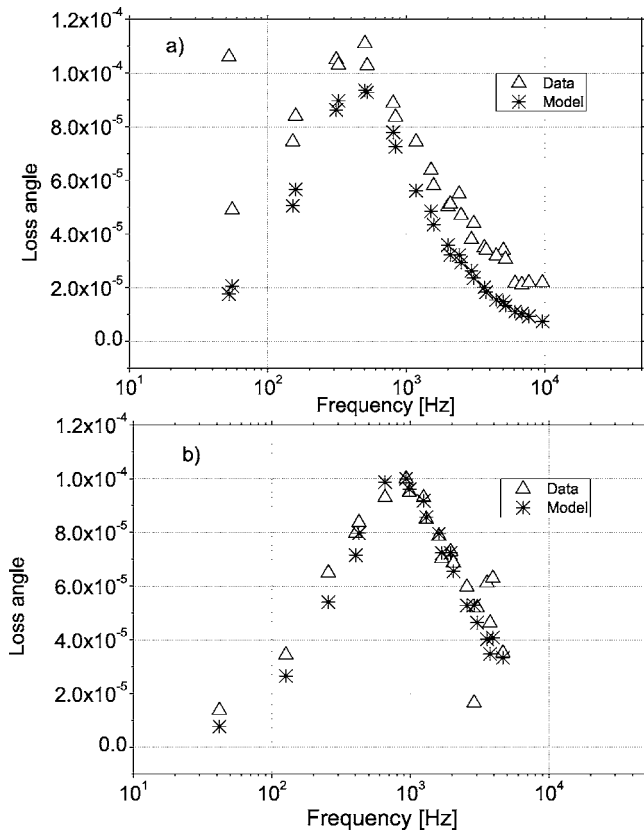


FIG. 9. a) Measured loss angle of a 289 mm (free length) fiber, with an average diameter of 746 μm . The stars represent the thermoelastic contribution as predicted by the model described in the text; (b) measured loss angle for the same fiber after the etching process; the average diameter is now 574 μm , while the free length is 278 mm.

isotropic etch of the fiber it was used the so called HNA solution, a mixture of HF and nitric acid, diluted with water or acetic acid. The etching velocity was kept at a low level using a 75% HNO_3 , 20% HF, and 5% CH_3COOH solution.²⁹

In Fig. 9(b) the measured values of the loss angle for the same fiber after the etching process are shown. The diameter reduction shifts the position of the thermoelastic peak to higher frequencies. A comparison of these values with the thermoelastic losses, computed as previously described, shows that excess losses play no significant role anymore, thus confirming the surface contamination hypothesis. A small excess is still found at low frequencies: this is probably due to clamp losses.

Figure 10 shows the measured values of ϕ for another 111.5 mm long fiber treated with chemical etching. Since this fiber has a roughly elliptical section, it is evident the presence of two sets of modes corresponding to the different lengths of the two ellipse axes. An unloaded cylindrical fiber, clamped at the upper edge, shows a set of resonance frequencies f_i given by

$$f_i = \frac{1}{2\pi} \sqrt{\frac{EI}{\rho S}} k_i^2, \quad (6)$$

with

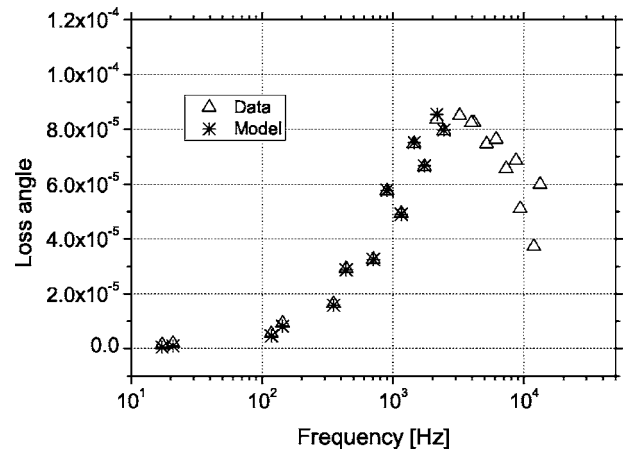


FIG. 10. Measured values of ϕ for a 111.5 mm long fiber after the etching process. The average diameter is 242 μm .

$$k_i = \frac{\alpha_i}{L}, \quad \alpha_i = \begin{cases} 1.8755 & i = 1 \\ \left(i - \frac{1}{2}\right)\pi, & i > 1 \end{cases}, \quad (7)$$

where I is the cross section moment and ρ the material density. By requiring the agreement of the resonance frequencies predicted by the fiber model with the measured ones, it is possible to fit the value of Young's modulus. For this fiber $E = (150 \pm 11)$ GPa with the error coming from the diameter uncertainty. This value is between what is expected for $\langle 100 \rangle$ and $\langle 110 \rangle$ crystallographic directions. The quantity f/k^2 depends only on Young's modulus and on the geometry of the fiber. In Fig. 11 the measured values of f/k^2 for the 111.5 mm long fiber versus the mode number are shown. Data follow two different trends, reflecting the ellipticity of the fiber section; the values are not constant since the fiber geometry is irregular. The figure shows also the values predicted by the finite elements analysis. The agreement between data and prediction is very good: Since the model consider a fiber whose properties are constant along the length, it is possible to conclude that the geometry of the fiber is kept into account properly and that any variation of Young's modulus should be small. Using finite element analysis it is also possible to identify some modes which are not purely transversal; these are not used in the thermoelastic

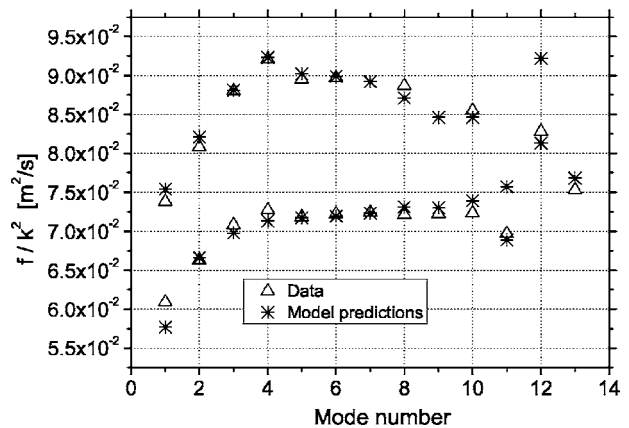


FIG. 11. Values of f/k^2 for a fiber with a roughly elliptical section.

TABLE I. Measured parameters for two different Si fibers.

L (mm)	E (GPa)	α (K ⁻¹) 10 ⁻⁶	κ [W/(m K)]	c
111.5±0.5	150±11	2.54±0.13	146±13	0.018±0.002
308.0±0.5	174±12	2.56±0.11	138±11	0.001±0.001

analysis since there is not a simple model of the loss angle for these situations. The thermal expansion linear coefficient is completely determined by the thermoelastic peak amplitude [see Eq. (2)] using the known specific heat [707 J/(kg K)] and density (2330 kg/m³) of Si.²³ For this fiber $\Delta=(17.3\pm 0.2)\times 10^{-5}$. The error is due to the fact the thermoelastic peak is sampled only at the resonance frequencies and the maximum amplitude is estimated using the ϕ trend around the peak. Assuming for T the measured value of 293 K, $\alpha=(2.54\pm 0.13)\times 10^{-6}$ K⁻¹.

The τ_h parameter in the thermoelastic curve allows a determination of the thermal conductivity of the fiber. The heat flux characteristic time is

$$\tau_h = F \frac{\rho C_V d^2}{\kappa}, \quad (8)$$

where d is an effective distance for the heat flow and F is a geometrical constant keeping into account the shape of the fiber section. For this roughly elliptical fiber, an estimate of the distance d can be deduced for each mode assuming a cylindrically shaped fiber oscillating at that frequency. In this way the elliptical section is approximated with two circular sections, one with the larger axis as diameter and the other with the dimensions of the shorter axis, for the two main oscillating directions. Nevertheless the larger curvature radius assumed for the external circular section leads to underestimating the heat gradient and, consequently, to overestimating τ_h ; the opposite happens assuming the internal circular section. A better first-order estimation can be obtained modifying Eq. (8) with the introduction of a parameter c correcting the form factor F known for a cylindrical geometry,

$$\tau_h = \frac{1}{2.16} (1 \pm c) \frac{\rho C_V d^2}{\kappa}, \quad (9)$$

where the sign $+$ in front of c is used when the inscribed circular cross section is taken into account. For the 111.5 mm long fiber, the fitting parameters of Eq. (9) are $\kappa=(146\pm 13)$ W/(m K) and $c=(0.018\pm 0.002)$, considering only the pure transverse resonance modes. The errors on the parameters κ and c are evaluated varying E and α within their errors.

Table I summarizes the physical parameters measured for two different fibers. The parameter c for the 308 mm fiber is compatible with zero, reflecting the almost circular shape of the fiber section.

Although obtained through an indirect measurement, the values of the linear thermal expansion coefficient α and of the thermal conductivity κ agree within the errors with those reported in literature.^{23,30,31} The measured values of Young's modulus confirm the fact the seed crystal orientation is not maintained constant along the fiber.

VI. MEASUREMENTS OF THERMOMECHANICAL PARAMETERS OF FIBERS AT LOW TEMPERATURE

A. Low temperature measurement apparatus

The cryogenic facility consists of a commercial cryostat supplied by Janis Research Co., where the sample clamping system is cooled by liquid helium. In the cryostat the sample is located under vacuum (10^{-5} mbar, measured at the outlet flange) and it is cooled down through a copper clamp. The effective temperature is set up, above 4.2 K, through a controller-resistor system. For this work only liquid nitrogen has been used to cool down the cryostat and then the lowest attained temperature is about 80 K. A large effort has been made to reduce the influence of the temperature variation in the clamping losses. In this case the fiber is kept in the copper clamp through a spring that should maintain the clamping pressure constant. The relationship between the clamping pressure and the dissipation in the suspension system has been investigated by some of the authors in Ref. 28, showing the direct dependence of the loss angle by the clamping pressure and the effectiveness of the monolithic design. The measurement technique is similar to the one used at room temperature and described in Ref. 10, but, to realize the shadow meter, a 100 mW HeNe laser was used as light source instead of a led. A beam-expansion telescope has been used to obtain a laser waist larger than the fiber diameter.

The longer fiber could not be hosted in the cryostat, thus the lower temperature measurements were performed on the 111.5 mm fiber.

B. Young's modulus temperature dependence

From the Material Properties Data Base²³ the temperature dependence of Young's modulus is known above room temperature and it varies strongly with the crystalline orientation. A semiempirical model has been developed by Wachtman *et al.*³²

$$E(T) = E(0) - BT e^{-T_0/T} \quad (10)$$

where $E(0)$ is the Young's modulus at $T=0$ K and B and T_0 are constant parameters; this model should be valid in a large temperature range. To evaluate Young's modulus at different temperatures, the mode frequencies of the fiber have been tracked down to 80 K. Not all the detectable resonant modes have been always excited and measured; for some intermediate temperature, only few key frequencies have been followed.

From Eq. (6) it is possible to link the relative resonant frequency variation $\Delta f_n(T)/f_n(T_{\text{room}})$ to relative Young's modulus variation $\Delta E(T)/E(T_{\text{room}})$:

$$\frac{E(T) - E(T_{\text{room}})}{E(T_{\text{room}})} = \frac{1}{N_{\text{modes}}} \sum_{n=1}^{N_{\text{modes}}} \frac{[f_n(T)]^2 - [f_n(T_{\text{room}})]^2}{[f_n(T_{\text{room}})]^2}. \quad (11)$$

The measured frequencies are reported in Fig. 12 and reconstructed Young's modulus variation in Fig. 13. As cited before, the behavior of Young's modulus above room temperature is well reported in literature.²³ Extrapolating these models below room temperature for the three silicon crystal

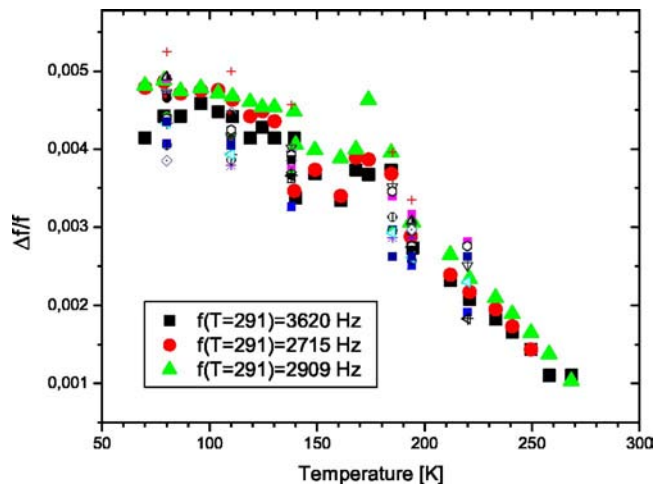


FIG. 12. Relative frequency variation vs temperature. For the three modes indicated in the figure all the frequency values have been recorded; for the other modes a subset of measurements has been performed.

orientations, it is possible to draw the three straight lines of Fig. 13. It is clear that the $\langle 110 \rangle$ orientation (dotted line) is excluded by the experimental data. This result, together with the $\langle 100 \rangle$ nature of the initial seed, confirms the dominance of the $\langle 100 \rangle$ orientation in the fiber. The solid curve in Fig. 13 is the fit of the model reported in Eq. (10) to the experimental data; the 0 K Young's modulus results to be $E(0) = 151 \pm 10$ GPa and the other two parameters are $B = 15.1 \pm 1.7 \pm 0.9$ MPa/K and $T_0 = 324 \pm 33 \pm 3$ K (the first error is due to the fit procedure and the second one to the room temperature determination error of Young's modulus), in good agreement with previous measurements³⁴ (according to Ref. 33 $T_0 \approx \Theta_D/2$ and the silicon Debye temperature is $\Theta_D = 645$ K). A similar analysis has been performed in another work.³⁴

C. Loss angle temperature dependence

Despite the efforts in realizing an experimental apparatus that permits to measure the thermoelastic dissipation in a

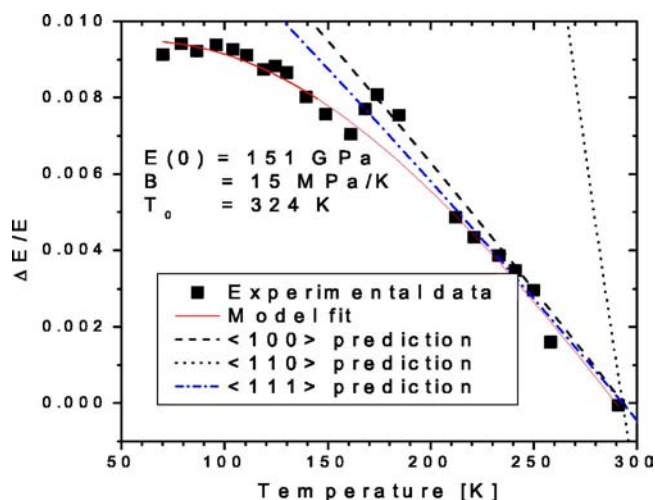


FIG. 13. Relative Young's modulus variation vs temperature. The three straight lines show the extrapolation, below room temperature, of Young's modulus behavior reported in Ref. 23 for the three crystal orientations: $\langle 100 \rangle$ dashed line, $\langle 110 \rangle$ dotted line, and $\langle 111 \rangle$ dash-dotted line. The solid line is the fit of the model in Eq. (10) to the experimental data.

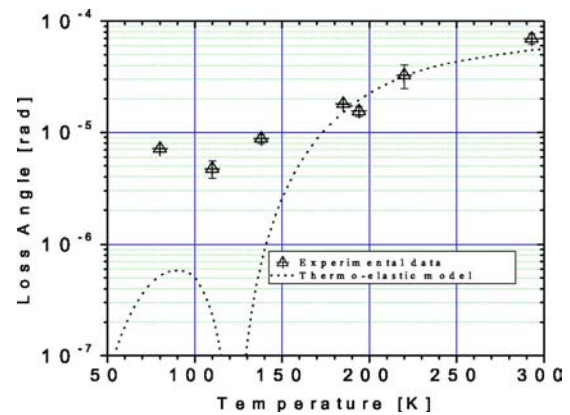


FIG. 14. Temperature dependence of the 6680 Hz mode vs temperature. The superimposed curve represents the expected loss angle due to thermoelastic dissipation in a silicon fiber having an average diameter of about 291.6 μm .

wide frequency range, the experimental data that have been recorded are affected by excess losses below the thermoelastic peak (about 3 kHz). For this reason, to determine preliminarily the temperature dependence of the loss angle, a mode with frequency well above the thermoelastic peak has been selected (6680 Hz at $T=291$ K), where the loss angle measured in the cryogenic apparatus coincides with the one measured in the room temperature setup. More efforts will be devoted to minimize clamping and recoiling losses in a future data taking session. In Fig. 14 the measured loss angle is compared with the expected curve due to the thermoelastic dissipation. The agreement is good down to about 160 K, then a huge excess loss is measured. This loss cannot be completely accounted by surface losses, assuming a constant frequency dependence model. In the one developed by Grettarsson and Harry,³⁵ the surface contribution ϕ_{surf} to the loss in a fiber is

$$\phi_{\text{surf}} = \mu \frac{h\phi_s}{VS}, \quad (12)$$

where $\mu=2$ is a geometrical parameter, h is the thickness of the dissipative surface, V is the specimen volume, and ϕ_s the loss angle of the material composing the surface layer. In the cryogenic apparatus, at frequency below the thermoelastic peak, it has been possible to measure loss angles lower than 10^{-6} in the present fiber. For this reason, the factor limiting the loss angle in Fig. 14 above 4×10^{-6} cannot be only due to surface losses. Similar results have been obtained in a previous work³⁴ using silicon cantilever blades. Comparing Fig. 14 of this work with Figs. 5 and 6 of Ref. 34 it is possible to say that the temperature dependence of the measured loss is qualitatively the same. It should be noted that other authors measured a broad dissipation peak at about 160–170 K for megahertz resonating microcantilever springs,³⁶ at 130–140 K for kilohertz resonating microcantilever springs,³⁷ or at about 115 K for single-crystal silicon cylinders;²⁰ all these phenomena have been interpreted as dissipation due to surface defects, bulk dislocations, or surface oxidation. In our work we have no evidence of these peaks but rather of a plateau as the temperature drops below 150 K. This behavior can be justified by a dominating excess loss that will be investigated and possibly reduced in the near

future. Measurements of mechanical loss in silicon cylinders have been recently performed by another group³⁸ and a similar plateau at a level of about 7×10^{-8} , between 100 and 200 K, can be observed. The difference on the two plateau levels could be explained with the different sample size; in fact, thanks to the Eq. (12), the surface losses are proportional to the inverse of the sample radius. The radial dimension of the silicon sample used³⁸ is about two orders of magnitude larger of the fibers used in this test and this could easily explain the lower plateau level.

VII. DISCUSSIONS

The goal of this article was to characterize the thermo-mechanical properties of crystalline Silicon fibers produced by μ -pulling technique and to analyze their advantages and drawbacks in the realization of a low thermal-noise suspension for a future interferometric gravitational wave detector. The production technique and the etching procedure described in the article permit to realize fibers having the appropriate size, but a better control of the diameter regularity and crystal orientation must be developed. Nevertheless, at room temperature, the produced fibers confirm the expected properties: The high thermal conductivity of silicon pushes the thermoelastic dissipation peak at high frequency, as it is evident comparing Fig. 9(b) with Fig. 4. The technical difficulties in this new production procedure, however, make the silicon fibers still less appealing respect to fused silica fibers; in fact, the fused silica fibers drawing technique is well advanced now and the thermal-noise performances are, in the frequency range of interest, comparable. At low temperature (about 120 K), if the preliminary results reported in this work (Fig. 14) will be confirmed by more accurate measurements, the reduction of the thermoelastic dissipation, due to the thermal expansion coefficient behavior, is hidden by the presence of other dissipation mechanisms, some of them related to bulk and surface defects. This result suggests to investigate the behavior of a crystalline Silicon fibers suspension at really cryogenic temperature (about 5–20 K) where the thermo-elastic dissipation will be negligible thanks both to the vanishing of the thermal expansion coefficient and to the direct temperature dependence of the thermoelastic strength Δ [see Eq. (2)].

ACKNOWLEDGMENTS

The authors wish to thank Dr. M. Porrini, Professor T. Fukuda, and Dr. A. Yoshikawa for helpful discussions and suggestions. This work has been supported by INFN, in the Virgo R&D program, by the European Commission, in the FP6 framework (project ILIAS, research activity JR3-

STREGA) and by the Italian Ministry of the University and Research (MIUR-PRIN-2002).

- ¹A. Araya *et al.*, *Proceedings of the TAMA Workshop on Gravitational Wave Detection, Saitama, Japan, 12–14 November 1996*, edited by K. Tsubono, M. K. Fujimoto and K. Kuroda, (Universal Academy, Tokyo, 1996), pp. 55–62.
- ²D. Coine, IEEE Aerospace Applications Conf. Proc. **4**, 31 (1996).
- ³J. Hazel, S. Kawamura and F. Raab, LIGO Document No. T960074–07-D, 1996 (unpublished); available at <http://www.ligo.caltech.edu/docs/T/T960074-07.pdf>
- ⁴G. Cagnoli, L. Gammaitoni, J. Kovalik, F. Marchesoni and M. Punturo, Rev. Sci. Instrum. **71**, 2006 (2000).
- ⁵F. Acernese, Class. Quantum Grav. **21**, S425 (2004).
- ⁶B. W. Barr *et al.*, Class. Quantum Grav. **19**, 655 (2002).
- ⁷V. B. Braginsky, V. P. Mitrofanov and K. V. Tokmakov, Phys. Dokl. **40**, 564 (1995).
- ⁸S. Rowan, R. Hutchins, A. McLaren, N. A. Robertson, S. M. Twyford and J. Hough, Phys. Lett. A **A227**, 153 (1997).
- ⁹C. Zener, *Elasticity and Anelasticity of Metals* (University of Chicago Press, Chicago, 1948).
- ¹⁰G. Cagnoli, L. Gammaitoni, J. Kovalik, F. Marchesoni and M. Punturo, Phys. Lett. A **255**, 230 (1999).
- ¹¹P. Amico *et al.*, Rev. Sci. Instrum. **73**, 3318 (2002).
- ¹²S. D. Penn *et al.*, (to be published) Phys. Rev..
- ¹³C. Zener, Phys. Rev. **53**, 90 (1938).
- ¹⁴G. Cagnoli and P. A. Willems, Phys. Rev. B **65**, 174111 (2002).
- ¹⁵S. Rowan, Proceedings of the Aspen Winter Conference on Gravitational Waves (1999) (unpublished) available at <http://www.ligo.caltech.edu/docs/G/000069-00.pdf>
- ¹⁶S. Rowan *et al.*, Proc. SPIE **4856**, 292 (2003).
- ¹⁷P. Amico *et al.*, Nucl. Instrum. Methods Phys. Res. A **518**, 240 (2004).
- ¹⁸P. Amico *et al.*, Class. Quantum Grav. **21**, S1009 (2004).
- ¹⁹S. M. Hu, J. Appl. Phys. **53**, 3576 (1982).
- ²⁰D. F. McGuigan *et al.*, J. Low Temp. Phys. **30**, 621 (1978).
- ²¹C. C. Lam and D. H. Douglas, Phys. Lett. **85**, 41 (1981).
- ²²J. Ferreira, *The Detection of Gravitational Waves* edited by D. G. Blair, (Cambridge University Press, Cambridge, 1993), pp. 116–168.
- ²³Material Properties Database (MPDB), <http://www.jahm.com>
- ²⁴D. H. Yoon, T. Fukuda, J. Cryst. Growth **144**, 201 (1994).
- ²⁵V. Chani, A. Yoshikawa, Y. Kuwano, K. Hasegawa, and T. Fukuda, J. Cryst. Growth **204**, 155 (1999).
- ²⁶P. R. Saulson, *Fundamentals of Interferometric Gravitational Wave Detectors* (World Scientific, Singapore, 1994).
- ²⁷P. D. Desai, J. Phys. Chem. Ref. Data **15**, 967 (1986); K. K. Kelley, US Bureau of Mines, Bull. 476, (1949).
- ²⁸G. Cagnoli, L. Gammaitoni, J. Kovalik, F. Marchesoni, M. Punturo, Phys. Lett. A **213**, 245 (1996).
- ²⁹S. K. Ghandi, *VLSI Fabrication principles* (Wiley, New York, 1994).
- ³⁰C. A. Swenson, J. Phys. Chem. Ref. Data **12**, 179 (1983).
- ³¹C. Y. Ho, R. W. Powell and P. E. Liley, J. Phys. Chem. Ref. Data **1**, 279 (1972).
- ³²J. B. Wachtman *et al.*, Phys. Rev. **122**, 1754 (1961).
- ³³U. Gysin *et al.*, Phys. Rev. B **69**, 045403 (2004).
- ³⁴S. Reid *et al.*, in Proceedings of 22nd Texas Symposium on Relativistic Astrophysics at Stanford University, 13–17 December 2004, (unpublished).
- ³⁵A. M. Gretarsson, G. M. Harry, Rev. Sci. Instrum. **70**, 4081 (1999).
- ³⁶S. Evoy *et al.*, Appl. Phys. Lett. **77**, 2397 (2000).
- ³⁷K. Y. Yasumura *et al.*, J. Microelectromech. Syst. **9**, 117 (2000).
- ³⁸R. Nawrodt, Proceedings of the second ILIAS-GW Annual Meeting, Palma de Mallorca (2005) (unpublished), available at http://www.ego-gw.it/ILIAS-GW/documents/Palma_Talks/STREGA/2005-ILIAS-PdM-Jena.pdf